Programmable Sponge for Hydro-Active Morphing Module with Light Weight and High-Volume Change

*Hajun Lee, Tianyu Yu, Mingjie Zheng, David Jourdan, Yuxuan Sun and Lining Yao**

Department of Mechanical Engineering
University of California, Berkeley, CA 94720, USA
* Corresponding Author E-mail: liningy@berkeley.edu

Keywords: cellulose sponge, soft robotics, shape-morphing structure, aquatic devices

Abstract

Sponge materials offer a unique combination of porosity, flexibility, compressibility, and responsiveness, yet their potential as primary elements in shape-morphing systems remains underexplored. Here, we present a modular shape-morphing platform constructed entirely from pre-compressed cellulose sponges, referred to as "foambots." Each block is geometrically patterned to induce anisotropic swelling, enabling programmable volumetric morphing upon hydration without external power or electronics. By stacking and orienting foambots in controlled configurations, we create complex three-dimensional structures capable of untethered transformation in aquatic environments. The large volumetric expansion (~1:10 before and after morphing) allows for unique compact form for easy transport and deployment. We systematically investigate how key design parameters (block length, hole position, and orientation) govern bending behavior, and demonstrate inverse design strategies to achieve target geometries. Using this approach, we realize two functional applications leveraging foambots's programmable large volumetric expansion for deployable floating structures: a wearable flotation module that wraps around the user's limb, and a self-propelling boat capable of expanding ~463% of its original size when deployed, autonomous deploying, and traveling on water. These results establish cellulose sponge as a unique, sustainable material for morphing applications and introduce a scalable, low-cost strategy for creating deployable and reconfigurable soft structures.

1. Introduction

Sponge materials, characterized by their highly porous and interconnected architectures, have been widely used in diverse applications ranging from cleaning tools to biomedical scaffolds.[1–7] Their open-cell morphology enables rapid liquid uptake and retention, while the compliant structure accommodates large, reversible deformations such as bending, twisting, expansion and compression.[8–13] This combination of attributes makes sponges attractive candidates for applications requiring environmental responsiveness and mechanical compliance.[14–16]

Leveraging these advantages coming from their porous structure, sponge-like materials have been broad adopted across a range of research fields. Their porous matrix not only facilitates fluid handling but also allows for the incorporation of functional or stimuli-responsive substances, supporting the development of multifunctional systems.[17–20] In soft robotics, for example, sponge materials have been integrated as compliant interfaces or cushioning elements, often attached externally to robot bodies or embedded within jamming actuators to provide passive shape modulation.[21–26]

Beyond such structural or mechanical roles, recent studies have further expanded the functional landscape of sponge systems by engineering sponges from elastomers or hydrogels and combining them with functional structures or responsive materials.[27–29] These engineered composites have been tailored for diverse applications such as tuning fluid absorption rates via structural programming, enabling temperature-triggered squeezing through thermo-responsive gels, and achieving stiffness modulation using embedded low-melting-point alloys (LMPAs).[3,4,30] Other notable demonstrations include ethanol-infused sponges that act as artificial muscles, porous sensing matrices for thermal and tactile feedback, and morphable robots actuated by temperature-driven phase switching.[31–33] These examples collectively underscore the versatility of sponge-based platforms as adaptable and functional components in advanced material systems.

While sponge-like materials have demonstrated effectiveness as substrates or structural matrices for embedded functionalities, their role has largely remained auxiliary. In most cases, they serve as compliant carriers for embedded sensors, actuators, or diverse functional materials, rather than acting as the primary driver of morphological change.[34–40] Consequently, the sponge itself has rarely been harnessed as a standalone, programmable, and designable material platform capable of autonomous shape-morphing. The prevailing paradigm has treated sponges as soft scaffolds that are compressible, absorbent, and structurally passive, rather than as actively deformable modules capable of structural transitions triggered by simple environmental stimuli such as hydration.

Several studies have demonstrated that silicone-based sponge structures incorporating bilayer architectures can achieve shape-morphing behavior through differential volumetric expansion between layers. [27,41,42] However, these systems inherently rely on the bilayer mechanism, and their performance in terms of swelling magnitude in aqueous environments and design scalability remains limited due to constraints imposed by the materials and fabrication processes. As a result, realizing large, complex, and scalable shape transformations in water-based environments remains challenging.

In this context, cellulose sponge emerges as a uniquely promising yet underexplored material platform for environmentally triggered shape-morphing. Commercial cellulose sponges, commonly found in household products, are lightweight, biodegradable, and derived from renewable biomass.[43,44] In the dry state, they remain compact and stiff. Upon exposure to water, they swell substantially and soften, undergoing large-scale dimensional and mechanical transitions rapidly. Importantly, unlike synthetic hydrogels or elastomeric foams that often require specialized processing or curing, cellulose sponges can be easily cut, shaped, and assembled using standard fabrication tools.[45–49] This accessibility, along with their low cost and recyclability, makes cellulose sponge an appealing platform for scalable and sustainable morphing systems.

Here, we present a modular shape-morphing platform composed entirely of cellulose sponge building blocks, hereafter referred to as “foambots.” Each foambot consists of a small sponge block that is geometrically patterned to induce anisotropic swelling when hydrated. These individual sponge blocks are called “foam blocks” throughout this paper. By selectively constraining expansion at predefined locations, we encode programmable curvature and anisotropic deformation into individual units. Furthermore, by stacking and orienting multiple foambots in controlled configurations, we realize composite structures capable of complex morphing behaviors such as bending, twisting, and coiling across multiple spatial scales. This layer-by-layer assembly strategy enables the construction of large-scale, untethered systems that can autonomously reconfigure in response to water exposure without requiring embedded electronics or external power inputs. Our work therefore demonstrates a new design paradigm in which sponge blocks are used not as passive carriers, but as active morphing elements in their own right.

To validate this concept and systematically explore the design rules governing foambot behavior, we first investigate how key design parameters, namely block length, hole position, and orientation, affect bending performance. Through image-based measurements and simple geometric analysis, we quantify how asymmetric swelling translates into macroscale curvature.

We show that hole position is critical in determining curvature magnitude, while orientation controls the global geometry. The result is a versatile design palette from which we can construct a wide variety of morphing structures.

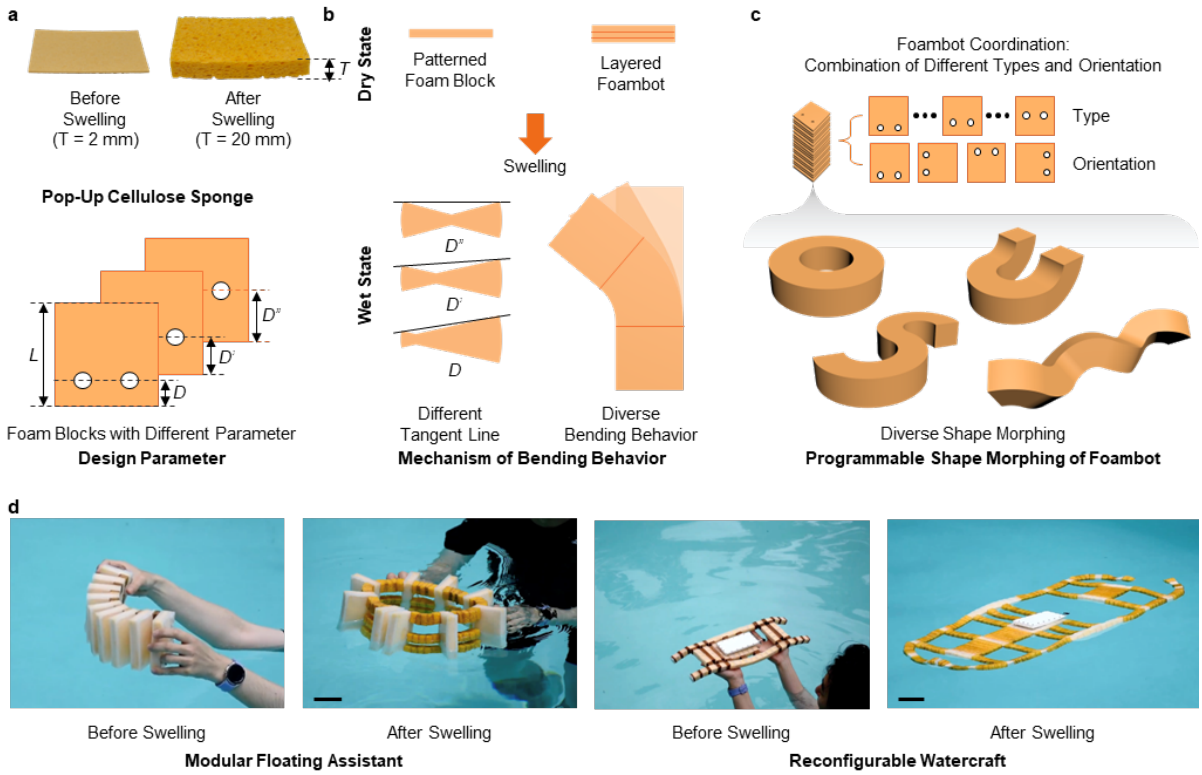

Figure 1. Overview of our foambot system. Programmable, foam-based platforms enabling aquatic shape-morphing applications. a) Volumetric expansion behavior of cellulose sponge and design parameters used for programming individual foam blocks. b) Bending behavior of foambots derived from deformation of individual foam block. c) Diverse structures achievable through reconfiguration of the foambot based on segmental coordination. d) Pictures describing the applicability of foambots in aquatic environments. All scale bars, 10 cm.

An overview of our foambot system is presented in **Figure 1**, which outlines the fundamental material behavior, the design logic for programming foam blocks, and the resulting application scenarios. As shown in Figure 1a, the foundation of the system lies in the volumetric expansion behavior of commercially available cellulose sponge. When dry, the sponge remains compact and stiff, but upon hydration, it undergoes rapid and substantial volume expansion, providing a passive, energy-free actuation mode. This property enables the design of morphable modules by embedding geometric constraints.

To achieve anisotropic deformation, we introduce hole patterns into individual foam blocks at varying distances from the foam block's edge, using a 1 mm-diameter biopsy punch. These holes restrict local swelling in a controlled region, resulting in asymmetric expansion. As shown schematically in Figure 1b, when the block swells, the height difference between the two outer edges around the punched region generates curvature. By adjusting the distance of hole position relative to the foam block's edge, we can produce a range of deformed geometries with varying height differentials, leading to different bending angles (Video S1, Supporting Information). This predictable bending response forms the core actuation mechanism of the foambot and allows each foam block to be programmed to bend in a specific direction and magnitude based on its hole pattern and geometry.

Building on this principle, diverse morphing structures can be constructed by stacking multiple programmed foam blocks with varying orientations, as illustrated in Figure 1c. Using an inverse design approach, we mapped desired final geometries (e.g., arcs, circles, helices) to corresponding layer-by-layer foam block coordinations. This programming logic enables both 2D and 3D shape morphing, supporting scalable and reconfigurable designs. Based on this process, we demonstrate several foambots exhibiting distinct shape-morphing capabilities.

Finally, we demonstrate the practical utility of the foambot platform as shown in Figure 1d, which showcases two representative aquatic applications: (1) a wearable flotation module generating a ring-like shape that can wrap around the user's limbs after deployment, and (2) a self-propelling aquatic robot equipped with a modular propulsion unit and capable of undergoing large-scale shape transformation. Both demonstrations validate the feasibility of our approach in real-world, water-based scenarios, showcasing functional behaviors such as automatic unfolding, passive deployment, magnetic self-locking, and directional locomotion.

Beyond technical capabilities, this work highlights the potential of cellulose sponge as a smart building block for sustainable shape-morphing devices. Unlike traditional smart materials, sponge blocks are biodegradable, recyclable, and affordable, and they offer fast, reversible swelling behavior without requiring active energy input. These properties make them ideal for disposable, compact, and adaptive devices, particularly in the context of environmental or safety applications where simplicity and scalability are key.

In summary, our work presents a new paradigm for constructing reconfigurable aquatic systems using simple, sustainable materials and straightforward fabrication techniques. The foambot platform bridges the gap between passive swelling behavior and programmable structural morphing, offering a scalable and eco-friendly alternative to complex soft robotics. With further optimization in design precision, reversibility, and integration of multifunctional materials, the

foambot system has the potential to drive innovation across a wide range of domains, including disaster relief, environmental monitoring, deployable structures, and wearable safety gear.

2. Fabrication of Foambots

The fabrication process of the foambot consists of four main steps: material preparation, hole punching, glue injection, and block assembly, as illustrated in **Figure 2**a. Commercially available cellulose sponges were used as the base material. These dried and compressed sponges were utilized in their as-received condition.

Material preparation involved two procedures: cutting the sponges and fabricating hole templates. Sponges were cut into small blocks using a laser cutter according to the required dimensions. In this study, these are referred to as foam blocks, typically measuring 20 mm × 20 mm, except in cases where foambots were used for parameter testing or as structural support components. Hole templates with various hole patterns (Figure S1, Supporting Information) were 3D printed to guide hole punching, which is critical for programming the bending behavior of the foambot.

Foam blocks were aligned with the hole templates, and two holes were manually punched into each block using a biopsy punch with a 1 mm diameter, following the predefined hole pattern. An elastomer was then injected into the holes, functioning as an internal adhesive. This glue anchored the upper and lower regions of the foam block around the punched area, mechanically constraining expansion in that region during swelling. By locally restricting expansion near the holes, bending behavior could be programmed into the foambot.

To assemble the blocks into a foambot, additional elastomer was applied to the contact surfaces between adjacent patterned blocks, which were then aligned and cured in a stacked configuration. Elastomer injection and block assembly could be performed either simultaneously or in separate steps. The ends of the foambot were sealed with various terminal components depending on the intended function, such as unpatterned foam blocks, buoyancy blocks (Figure S2, Supporting Information), elastomer plates, or permanent magnets encapsulated in elastomer (Figure S3, Supporting Information).

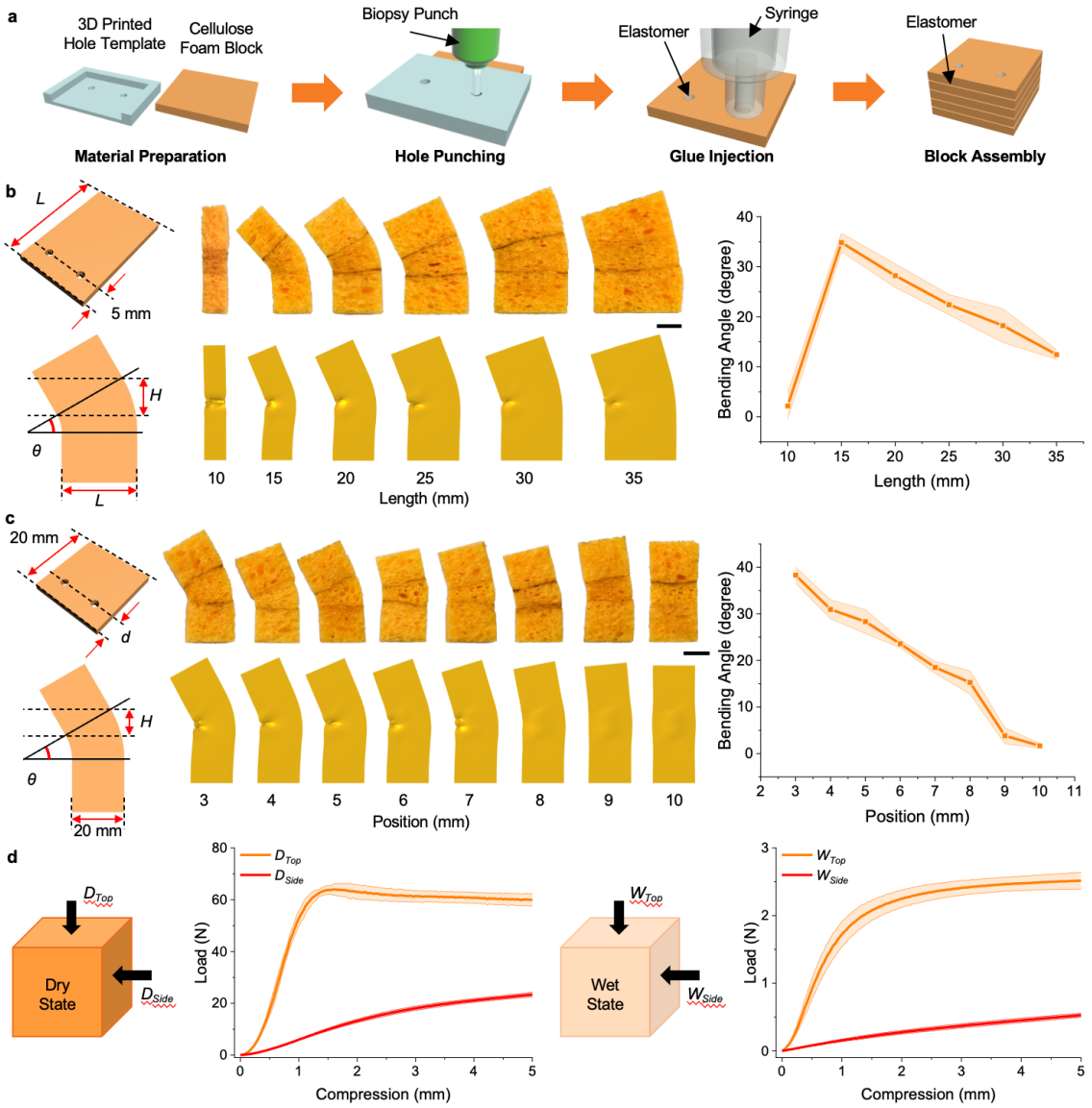

Figure 2. Fabrication and characterization of foam blocks. a) Schematic of the foam block fabrication process. b) Effect of foam block length (*L*) on bending behavior, under a fixed hole position. Blue lines indicate hole position. c) Effect of hole position (*d*) on the bending behavior of the foambot, represented by the distance from the edge of the foam block to the center of the punched hole. Blue lines indicate hole position. d) Compression test results of swollen foam blocks in both dry and wet states. *D* and *W* indicate the dry and wet states, respectively. "Top" refers to the direction parallel to the foam block's swelling axis, while "Side" indicates the direction perpendicular to the swelling axis. For each design parameter, N = 3 independent samples were tested, and data are presented as mean ± SD. All scale bars, 1 cm.

3. Design Parameters of the Foambot

We investigated the design parameters of the foambot by varying two key factors: the length of the foam block and the hole position. To perform this analysis, a series of three-layer foambots was fabricated by assembling a patterned foam block, programmed with specific hole positions, between two unpatterned foam blocks. The bending behavior of these foambots was analyzed via image processing after swelling, using photographs of their final deformed configurations. The bending angle was determined by extending the interfaces between the patterned and unpatterned foam blocks and calculating the angle between these extended lines. This was achieved by manually drawing lines on the images using PowerPoint, extracting the coordinates of each line's endpoints with a macro script, and computing the angle geometrically.

3.1. Effect of Foam Block Length on the Bending Angle of Foambots

Figure 2b shows the effect of foam block length on the bending behavior of the foambot. The block length (denoted as L) was varied from 10 mm to 35 mm, while the width (20 mm) and the hole position (5 mm from one edge) were kept constant.

When L = 10 mm, no bending behavior was observed due to the symmetric swelling induced by the centrally located hole. At L = 15 mm, the foambot exhibited the highest bending angle (~35°), indicating the greatest asymmetry in swelling. As the foam block length increased beyond 15 mm, the bending angle gradually and linearly decreased, as described in the bending angle vs. length plot in Figure 2b.

This trend can be explained by the geometric relationship between the vertical expansion at the ends and the horizontal length of the foam block. As illustrated in Figure 1b, the bending angle (θ) is primarily governed by the incline formed by the edges of foam block, specifically, approximated as the arctangent of H/L, where H is the vertical height difference between the peaks and L is the block length. While the vertical expansion height at the ends remained relatively consistent across samples, increasing L led to a shallower incline, thereby reducing the bending angle. This relationship is evident in the experimental images and simulation data presented in Figure 2b.

However, this trend holds only when the hole constraint does not significantly suppress expansion at the ends. When the foam block is too short, the influence of the anchored hole extends across a larger portion of the block, thereby reducing the effective expansion height and leading to symmetric or suppressed deformation. As a result, under a fixed hole pattern, the bending angle of the foambot is inversely related to its length.

Although the highest bending angle was observed at L = 15 mm, we selected L = 20 mm as the standard foam block length for all subsequent designs. This choice was based on two practical

considerations. First, to ensure the structural integrity of the hole pattern, holes were not placed too close to the block edges. Considering the 1 mm diameter of the biopsy punch, the hole pattern was conservatively defined starting from 3 mm inward from the edge. Second, shorter foam blocks tend to offer a narrower programmable range and may experience incomplete expansion at the ends due to stronger constraints from the hole. The 20 mm length allowed for a programmable range of approximately 3–10 mm while still achieving the second-highest bending angle. Thus, the 20 mm × 20 mm foam block provided an optimal balance between deformation performance and hole placement flexibility and was adopted as the standard unit throughout this study.

3.2. Effect of Hole Pattern on Bending Angle of Foambot

We further investigated the influence of hole position on the bending behavior of the foambot, as shown in Figure 2c. In this study, the foam block length was fixed at 20 mm, and the position of the punched hole (denoted as d) was systematically varied from 3 mm to 10 mm in 1 mm increments. Eight distinct hole patterns were tested under otherwise identical conditions.

The results revealed a clear dependence of the bending angle on the hole position. As the hole moved toward the center of the foam block (i.e., as d increased), the bending angle decreased in an approximately linear manner. When the hole was located at d = 10 mm, corresponding to the geometric center of the block, the foambot exhibited minimal bending, with the angle approaching zero. Conversely, when the hole was placed closer to the edge (d = 3 mm), the foambot exhibited its maximum bending angle, approximately 38°.

This trend can be attributed to the asymmetry in expansion introduced by the hole constraint. Holes positioned near the edge of the foam block create a stronger imbalance in swelling between the two sides, thereby inducing greater curvature. In contrast, centrally located holes result in more symmetric expansion, leading to negligible deformation. These findings are consistently supported by experimental photographs, simulation data, and the plotted trend in Figure 2c, all of which demonstrate a near-linear reduction in bending angle with increasing d.

3.3. Mechanical Properties of Foam Block Depending on the State

To assess the anisotropic mechanical properties of the sponge material used in the foambot, uniaxial compression tests were performed on foam blocks in two different states: fully swollen (wet) and swollen-then-dried. As shown in Figure 2d, the dried samples, although previously

swollen, exhibited substantially higher stiffness than their wet counterparts, regardless of the compression direction.

This increase in modulus upon drying enables the construction of foambots that are compact and mechanically stable in the dry state, while still capable of undergoing programmable transformation upon rehydration. In other words, the dried, compressed foam blocks provide structural rigidity and shape retention during fabrication and storage. Upon re-exposure to water, they re-expand and soften, allowing the foambots to spontaneously morph into their pre-programmed configurations without requiring any active control input.

Additionally, this behavior highlights a unique advantage of the cellulose sponge material: its dual-state nature offers not only sustainable, low-cost and lightweight fabrication, but also effective control over volume expansion and mechanical compliance. These features make the material particularly attractive for deployable and reconfigurable systems that benefit from compact storage and autonomous shape transformation upon activation.

4. Inverse Design Calculation and Diverse Shape-Morphing Structure of Foambots

We explored a range of shape-morphing structures achievable with foambots, including a ring, the letter “S”, a horseshoe, and a helix. **Figure 3** illustrates the inverse design process and the resulting shape-morphing behaviors. The fabricated foambots consisted of 12 to 16 layers of foam blocks, each with distinct hole patterns and orientations. In this work, we define the combination of hole pattern and layer-by-layer arrangement of foam blocks as the layer coordination of a foambot. This coordination was determined through a segment-by-segment inverse design procedure tailored to each target shape, as depicted in Figure 3a.

4.1. Inverse Design Calculation Procedure

We first derived the layer arrangement of foam blocks corresponding to specific target shapes through an inverse design approach. The process began with generating a target geometry in the form of a 2D or 3D spline curve. Next, in the case where the spline curve is three-dimensional (see horseshoe or helix examples) fabrication constraints require the curve to be segmented into piece-wise planar segments lying in one of 3 possible orthogonal planes (see Figure 3a: segmentation). This step is necessary because the square profile means planar segments can only be joined with discrete orientation shifts, in 90° increments (i.e., 0°, 90°, 180°, or 270°). The planar segments are then discretized into vertices and edges for length and curvature computation.

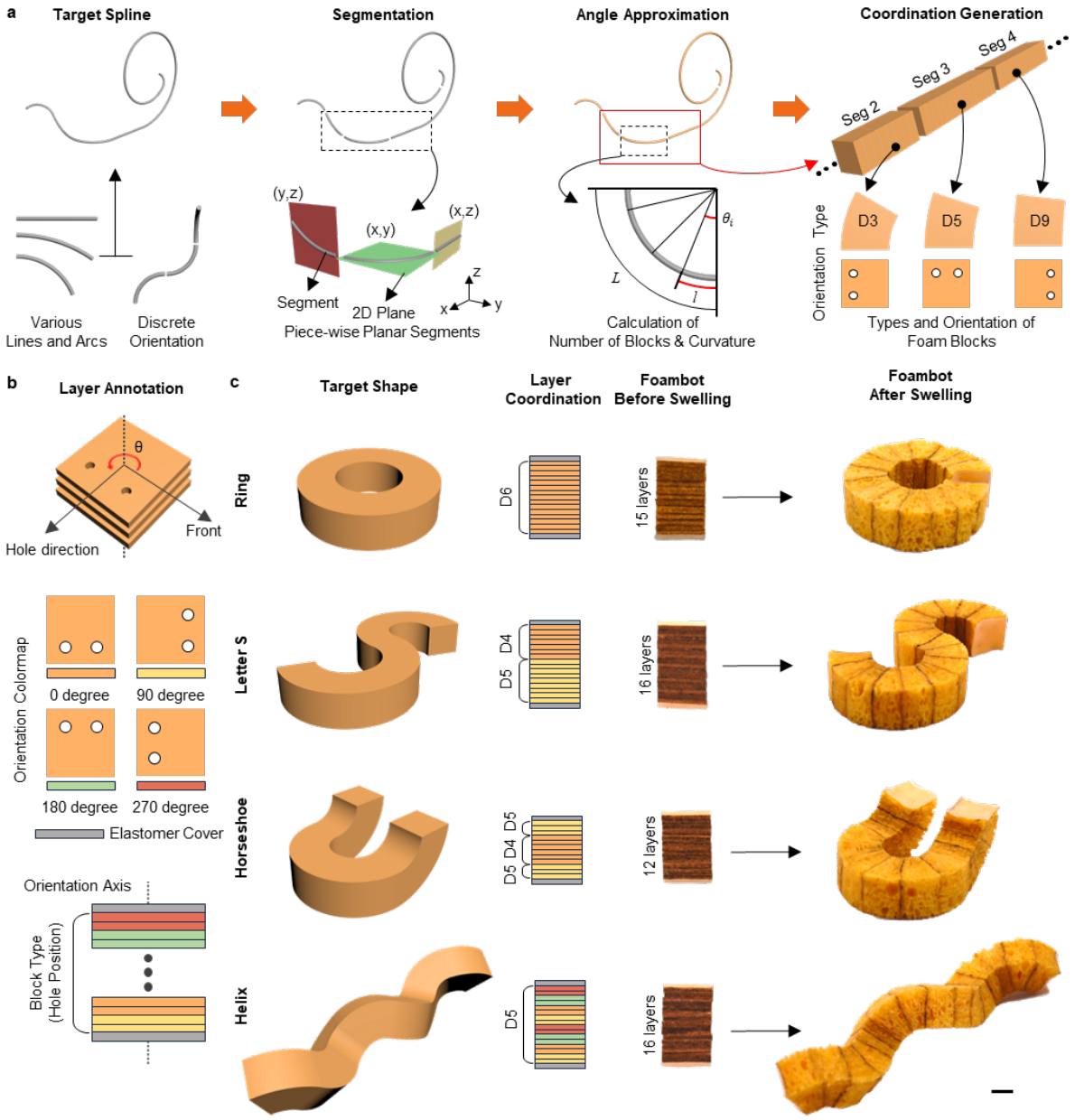

Figure 3. Inverse design calculation and demonstration of programmable swelling behaviors in foambots. a) Schematics illustrating the inverse design calculation process used to determine the segment-by-segment coordination of foam blocks required to achieve a specific target shape. b) Schematic showing the annotation method used to describe layer-by-layer configuration, including block types and their orientations. c) Left: Four representative target shapes (ring, S-shape, horseshoe, and helix) and the corresponding calculated foam block coordination. Right: Pictures of fabricated foambots before and after swelling. Each was constructed based on layer coordination obtained from the inverse design, demonstrating shape-morphing into the intended configurations. Scale bar, 1 cm.

For each segment, the total length L_{arc} was computed and divided by the average swollen length l_{arc} of a single foam block to estimate the number of required foam blocks as a real-valued quantity $N = L_{arc}/l_{arc}$. Since the physical construction requires N to be an integer, the input curve was uniformly rescaled to ensure that the computed value of N falls within ±0.15 of its nearest integer (e.g., 6.85–7.15 if rounded value of N is 7). The final number of foam blocks was then set to this nearest integer. This adjustment minimized geometric distortion while preserving the design curvature, enabling precise mapping of discrete foam blocks to the target shape.

The curvature assigned to each block j was computed from the discretization using the curvature formula by Bergou et al. [50]:

$$\kappa_j = \frac{1}{N_j}\sum_{i=1}^{N_j} 2\tan\left(\frac{\theta_i}{2}\right) \quad (1)$$

where θ_i denotes the turning angle at vertex i of the discretized curve, and N_j indicates the number of vertices corresponding to one foam block within a given segment. Based on the computed curvature, the hole position on each foam block was determined by inverting the curvature-to-hole position relation measured in Figure 2c for ranges of positions between 3 and 10 mm. A more detailed explanation of this procedure is provided in the "inverse design calculation" of the Experimental Section/Methods.

The types of foam blocks indicate the foam blocks with different position of hole. This type was labeled as D*n*, where *n* refers to the distance *d* (in mm) of the hole pattern from the edge to the center of the hole, as shown in Figure 2c. For example, D3 indicates the foam block with hole patten on 3 mm distance from the edge as shown in Figure 3a: coordination generation.

The final foambot layer coordination, comprising hole position and orientation, was then obtained by merging in sequence the result for each planar segment based on the relative orientation of their respective planes.

4.2. Layer Coordination Strategies for Shape-Morphing Foambots

The layer coordination obtained from the inverse design calculation was represented using the annotation scheme shown in Figure 3b, which encodes both the type and orientation of each foam block. The orientation of a given foam block layer was defined as the angle between the hole pattern direction and the arbitrarily designated front side of the foambot. To standardize this reference, the front direction was set based on the orientation of the hole pattern in the first layer. A colormap was used to indicate the orientation of each layer visually. In accordance with the inverse design calculation procedure described in Section 4.1, each foam block type was labeled as D*n*, where the subscript *n* indicates the distance of the hole pattern from the edge

of the block. For improved readability, consecutive foam blocks of the same type were grouped and annotated only once per continuous sequence.

We designed four different target shapes using the inverse design calculation: a ring, the letter "S", a horseshoe, and a helix, as shown in Figure 3c. Each schematic for the target shapes in Figure 3c illustrates the 3D rendering of the desired shape and its corresponding layer coordination. While the visualizations were rendered in 3D for clarity, all design data correspond to 2D spline-based curves used in the inverse design process.

The ring structure consisted of a single arc with a radius of 27.5 mm and required 15 D6-type foam blocks, all oriented in the same direction (0°). The letter "S" was constructed from two arcs with radii of 28 mm and 22.5 mm, respectively. Each arc was computed separately and then merged to form a single layer coordination. The larger arc used 9 D6-type foam blocks, and the smaller arc used 7 D5-type blocks, with a 180° rotational offset between the two segments.

The horseshoe shape was composed of three arcs: a central arc with a 22 mm radius and two side arcs with 23 mm radii. These required 6 D4-type foam blocks for the center and two sets of 3 D5-type blocks for the ends, attached with 90° rotational offsets. Lastly, the helix structure was formed from 8 arcs, each with a radius of 22 mm and sequentially rotated. Each arc used 2 D4-type foam blocks, totaling 16 blocks. The blocks were assembled such that their orientation rotated by 90° every two layers.

Next, we fabricated foambots based on the layer coordinations obtained from the inverse design calculations for the four different target shapes. To provide a constraining layer for the foam blocks placed at each end of the foambot, square-shaped silicone plates (20 mm × 20 mm × 1 mm) were attached, as indicated in the layer coordination diagrams. The structures of these foambots before and after swelling are shown in Figure 3c, and their final swollen shapes closely resembled the target configurations (Video S2-5, Supporting Information).

5. Applications

5.1. Modular Floating Assistant for Wearable Buoyancy Support

We developed a modular flotation device, termed the Modular Floating Assistant (MFA), by leveraging the shape-morphing behavior of the foambot for aquatic wearable applications. As illustrated in **Figure 4**a and 4b, each MFA module incorporates a foambot composed of two D6-type foam blocks alternately connected with three unpatterned foam blocks, forming a five-block layer coordination. Both D6-type foam blocks are aligned with the same orientation, as

shown in the layer coordination diagram in Figure 4b, while the unpatterned blocks are annotated as "N."

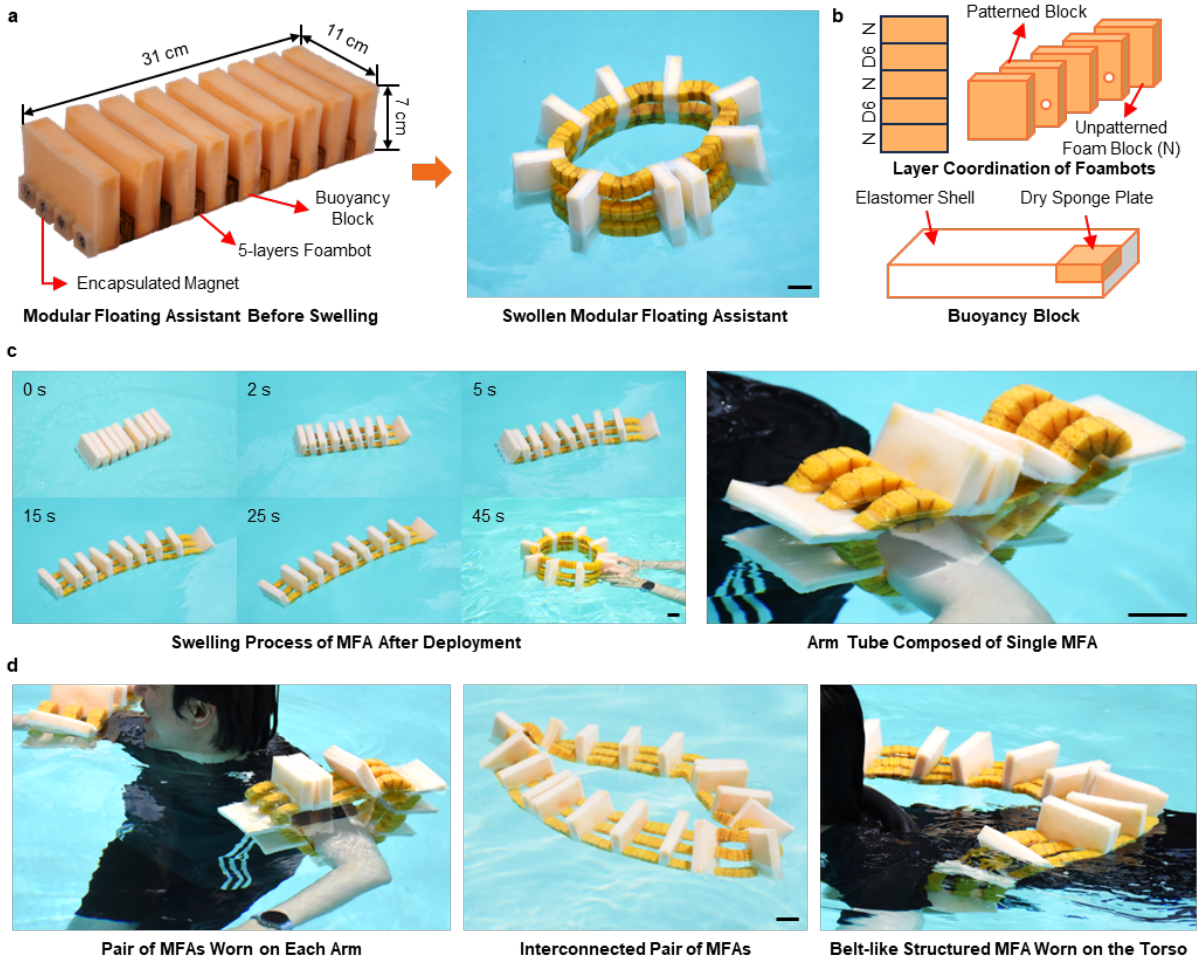

Figure 4. Modular floating assistants (MFAs). Application of the foambot as a reconfigurable system for personal flotation assistance. a) Structure of the MFA before and after deployment and swelling. Scale bar, 5 cm. b) Components of the MFA, including patterned foam bot and unpatterned blocks. The layer coordination of the foambot is displayed alongside its schematic. "D6" and "N" indicate a foam block with a hole pattern located at the 6 mm position and a foam block with no pattern, respectively. c) Sequential images showing the shape-morphing process of the MFA after deployment in water (left), and its wearable configuration as an arm-mounted flotation device providing buoyancy to the user (right). d) Pictures illustrating the wearable versatility and modularity of the MFA. A pair of MFAs can be independently worn on each arm (left), or magnetically interconnected to form an extended flotation assembly (middle). The resulting belt-like structure provides greater buoyancy and can be worn around the torso (right). All scale bars, 5 cm.

This foambot is affixed longitudinally along the side of a series of large buoyancy blocks, with its hole patterns oriented outward. Each MFA module comprises a total of nine large buoyancy blocks, bridged by three such foambots to provide programmed shape-morphing functionality. Additionally, four elastomer-encapsulated permanent magnets are embedded at both terminal buoyancy blocks, aligned with the foambot direction to facilitate magnetic self-locking.

Following deployment in water, the MFA undergoes a shape-morphing process that enables it to function as a wearable flotation device (Video S6, Supporting Information). The foambots swell rapidly upon hydration, with most of the expansion completing within approximately 25 seconds. Although the intrinsic bending behavior was designed to guide the structure into a ring-like configuration, the actual curvature is only partially expressed during swelling, as shown in Figure 4c. This limitation arises from the reduced mechanical strength and increased weight of the sponge in its swollen state, which prevents the structure from autonomously achieving full closure. To complete the transformation, the user manually brings the two ends together, allowing the embedded permanent magnets to engage and reliably secure the ring shape, which can then be worn around the arm or leg as a flotation module. To ensure reliable connection, the four magnets at each end are arranged with alternating north and south polarity, which prevents mismatched alignment and guarantees consistent pairing. Once formed, the ring-like module conforms comfortably to the user's arm or leg, offering localized buoyancy as a passive, wearable flotation assistant.

Beyond single-module use, the modularity and magnetic interlocking features of the MFA enable reconfiguration into larger systems. As demonstrated in Figure 4d, each MFA unit can function independently, for example, as a pair of arm-mounted devices, or be magnetically linked into a combined assembly. In this demonstration, two MFA units were connected to form a belt-like structure worn around the torso, illustrating how identical modules can be scaled and repurposed to accommodate different user needs. Although each foambot component is programmed for a specific shape-morphing behavior, the inherent softness of the swollen sponge allows for additional mechanical adaptability. Moreover, the MFA's straightforward construction, based on simple stacking and bonding of components, supports not only modular scalability but also the fabrication of larger, monolithic flotation structures. Such flexible and reconfigurable design space supports the development of versatile flotation systems for a range of aquatic safety and assistive applications.

5.2. Programmable Foamboat with Modular Propulsion System

Building upon the modular and reconfigurable principles demonstrated in the MFA system, we further extended the concept to construct a programmable watercraft, referred to here as the foamboat, as illustrated in **Figure 5**. We demonstrated both the substantial deployment-induced volume expansion and the active locomotion performance of the foamboat. This platform highlights how the integration of programmable foambot structures with a modular propulsion unit enables actively navigable devices, while also offering advantages in compact storage and efficient transport due to its minimized volume in the undeployed state (Figure S4, Supporting Information). Upon deployment, the structure autonomously transforms into a fully expanded configuration, underscoring its potential as a shape-morphing aquatic robot.

As shown in Figure 5a, the foamboat consists of reconfigurable foambots, small buoyancy blocks, and a modular propulsion system. The overall structure can be divided into four main sections: a U-shaped connector, bridge, body, and head/tail. The central body features a rectangular buoyant frame constructed from small foam blocks, referred to as the U-shaped connector. This connector includes four elastomer-encapsulated permanent magnets, which not only provide additional buoyancy over five times greater than that of the foam blocks (Figure S5, Supporting Information) but also enable attachment to the modular propulsion system via magnetic coupling. The U-shaped connector is linked to the bridge sections via bridge foambots. Each bridge connects the body to the head or tail, which also incorporate foambots integrated with buoyancy blocks for the stable floating.

Upon deployment in water, the foambots began to swell, triggering programmed expansion and bending that gradually transformed the structure into a boat-like geometry. To mimic the raised curvature commonly seen in the bow and stern of boats, the foambots in the head and tail segments were designed to undergo upward 3D deformation, as shown in Figure 5b. However, the final swollen structure exhibited a reduced height of approximately 3 cm, compared to the intended 5.5 cm in the 3D design schematic. This discrepancy is primarily attributed to the added weight from the encapsulated magnet blocks and water absorption, which amplified the influence of gravity and limited the achievable curvature. This arch-like 3D configuration was initially expected to reduce hydrodynamic resistance during locomotion by minimizing contact with the water surface. However, due to this reduced swollen height, this effect could not be experimentally confirmed under the current design and testing conditions.

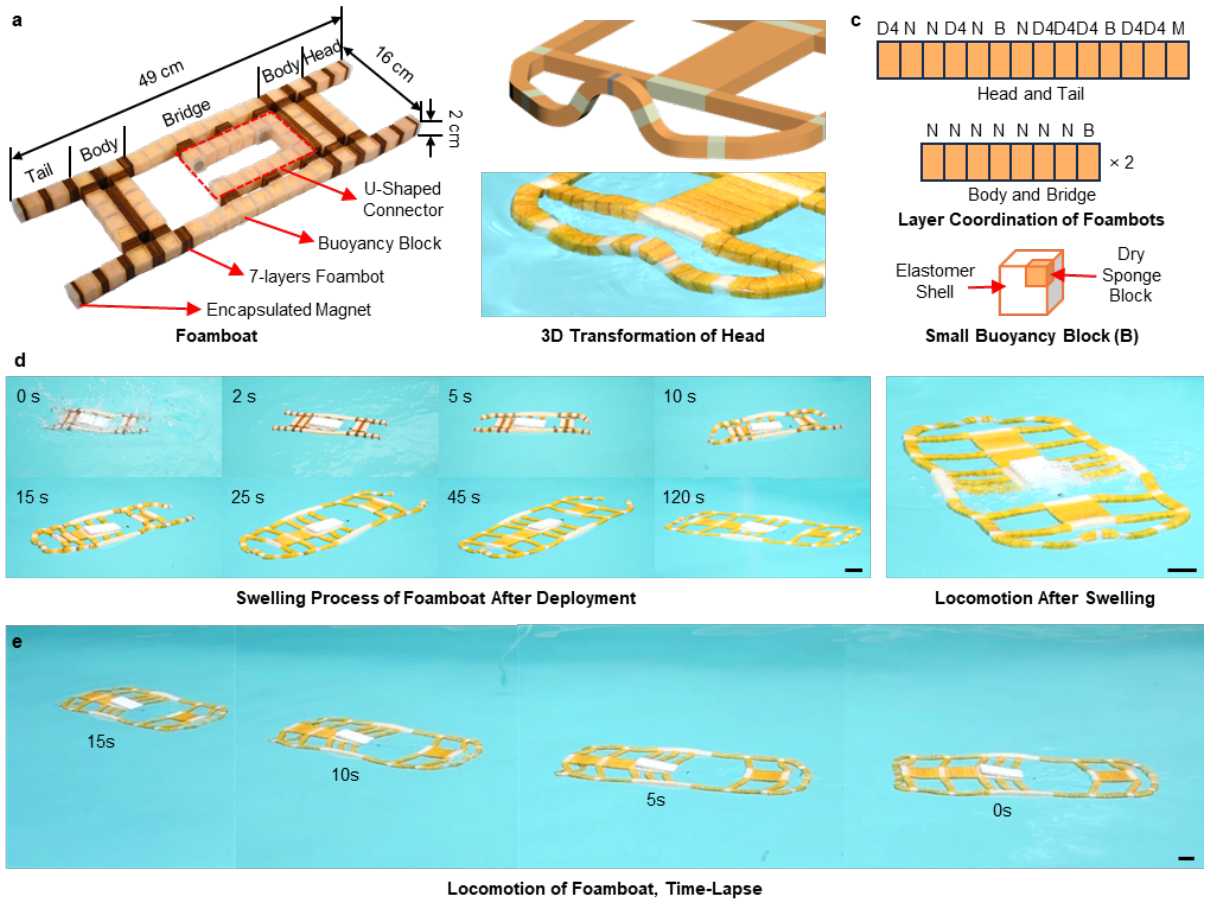

Figure 5. Foamboat with modular propulsion system. Programmable shape-morphing watercraft based on foam block assemblies. a) Overview of the foamboat composed of multiple foambot arrays and buoyancy blocks. b) Three-dimensional shape-morphing of the foambot head after swelling, compared with its 3D design schematic, highlighting the deviation in height caused by gravitational and hydration-induced effects. c) Foambot's layer coordination and structure of small buoyancy block, forming the foamboat. d) Sequential images illustrating the foamboat's shape-morphing process after being deployed in water (left), and its movement driven by the modular propulsion system once fully swollen (right). e) Time-lapse sequence of the foamboat's locomotion over 15 seconds. All scale bars, 5 cm.

At the end of the swelling process, pairs of foambots on each side of the head and tail spontaneously closed through a self-locking mechanism. To achieve this, elastomer-encapsulated permanent magnets were attached to the ends of the foambots in the head and tail segments, denoted as "M" in the layer coordination diagram.

The detailed layer coordination of each foambot used in the foamboat is illustrated in Figure 5c. For the head and tail, foambots generating 3D shape-morphing was installed, While the head and tail incorporated foambots programmed for 3D deformation, straight-expanding foambots

were used in the bridge and body sections. To improve structural stability during operation, an additional horizontal reinforcement was added at the center, linking the left and right sides while maintaining adequate buoyancy. Each structural module was fabricated by straightforward stacking and bonding of foam elements, following the modular design principles described earlier.

To provide locomotion, a detachable modular propulsion system was installed at the center of the U-shaped connector. This system unit comprises a motor, motor driver, propeller, and battery, adapted from a commercially available RC boat toy (Figure S6, Supporting Information). The propulsion module can be easily mounted or removed, allowing seamless interchangeability with foamboats of different sizes or shape-morphing characteristics depending on the application. A custom waterproof housing and lid were 3D-printed and sealed with a rubber gasket placed in a pre-designed concave groove, then secured using screws to ensure watertight protection.

The whole process of the shape-morphing process of the foamboat is illustrated in the time-lapse sequence in Figure 5d. While the majority of the shape-morphing process including hull formation was completed within approximately 45 seconds, hydration in the tail region was relatively slower, leading to final structural closure via magnetic self-locking around 120 seconds after deployment (Video S7, Supporting Information). After full deployment, the foamboat exhibited an expanded footprint of approximately 93 cm × 39 cm, corresponding to a ~463% increase in area compared to its initial compact form.

Subsequently, the modular propulsion system was activated, and the motor was wirelessly controlled via a handheld transmitter from a commercial RC toy system. Figure 5e displays a time-lapse sequence over 15 seconds, during which the foamboat traveled approximately 3 m across the water surface, achieving an average locomotion speed of ~20 cm/s. The motion remained stable with a generally forward trajectory, although a gradual rightward curvature was observed during locomotion (Video S8, Supporting Information). This deviation is presumed to result from a combination of factors including the strong thrust from the propulsion system, substantial hydrodynamic drag on the front, and slight structural deformation of the head section due to the relatively low buoyancy and mechanical softness of the swollen sponge. Nevertheless, the demonstration validates the system's ability to perform untethered aquatic locomotion.

6. Discussion

This study highlights a material-driven strategy for shape-morphing robotic platforms that offers unique advantages in large volumetric expansion, geometric programmability, simplicity,

accessibility, and environmental sustainability. By leveraging the intrinsic swelling behavior of cellulose-based sponge materials, and without relying on complex electronics or control systems, we enabled programmable deformation through low-cost and disposable foam elements. These foambots can be fabricated easily using modular stacking of predefined building blocks and achieve significant morphological transformations when exposed to water, making them particularly suited for aquatic and deployable applications.

Despite these achievements, several limitations remain. First, the current system relies on discretized orientation, where the assembly of foam blocks is limited to fixed rotational increments (e.g., 90°). This restriction reduces the resolution of curvature and can limit the ability to approximate smooth or organically curved structures. Secondly, shape reversibility remains a challenge. Although the sponge material remains compressible and can be re-dried, restoring the foambot to its original dry configuration, especially in complex or volumetrically expanded structures, is practically infeasible. This limitation constrains the system's reusability and resets capability in practical applications.

In addition, while we emphasized low-cost and sustainable materials, the use of elastomer as both adhesive and structural constraint poses a tradeoff in terms of full environmental sustainability. Developing and employing biodegradable or recyclable alternatives to elastomer would further improve the eco-compatibility of the system and enhance its alignment with sustainable design principles.

Nevertheless, the foambot platform offers significant room for expansion. Future directions may include integrating additional programmable actuation mechanisms to enable sequential reconfiguration, and refining the inverse design algorithm to support smoother curvature profiles with higher geometric resolution. One promising improvement is replacing the current square foam blocks with circular ones, which could enable continuous orientation rather than discrete steps. This adjustment would allow for more fluid and precise structural programming, facilitating advanced shape-morphing designs. Together, these developments could pave the way for more sophisticated reconfigurable aquatic robots and adaptive systems for environmental or safety applications.

7. Conclusion

In this study, we investigated the design principles and capabilities of a programmable, shape-morphing platform based on cellulose sponge materials, referred to as the foambot. By systematically analyzing the effects of key design parameters, such as block length, hole position, and layer orientation, we revealed how these variables govern the bending behavior

of individual foam blocks and, consequently, the overall deformation of assembled structures. Notably, orientation emerged as a critical degree of freedom that enables the construction of diverse 2D and 3D morphologies.

To support predictive and scalable design, we developed an inverse design algorithm capable of mapping a target shape into a layer-by-layer foam block coordination. This framework allowed for the realization of complex structures with programmable curvatures, demonstrating the effectiveness of the method in generating reconfigurable soft architectures.

Leveraging this approach, we developed two functional aquatic devices: a Modular Floating Assistant (MFA) and a self-propelling foamboat. These proof-of-concept demonstrations highlight the practical potential of our system in buoyancy assistance and deployable soft robotics.

Beyond their functional programmability, foambots also benefit from the intrinsic advantages of cellulose sponge as a material platform, such as lightweight, low-cost, sustainable, and capable of fast and large swelling. Altogether, these findings highlight the potential of foambots as a promising platform for constructing shape-morphing devices and reconfigurable systems in aquatic environments.

8. Experimental Section/Methods

Fabrication of Patterned Foam Block and Foambot

Commercial cellulose sponges (Amazon) were prepared and cut into blocks using a laser cutter (D1, xTool). Hole templates with various hole position guidelines were 3D printed (X1C and P1S, Bambu Lab) using polylactic acid (PLA) filament. Patterned foam blocks were fabricated by aligning each sponge block with a hole template and punching holes using a biopsy punch with a diameter of 1 mm, following the printed guideline. Elastomer (Ecoflex 00-30 and Dragon Skin 10 Medium, Smooth-On) was used as an adhesive to fill the holes in the foam blocks.

For foambot fabrication, individual foam blocks were stacked and bonded using elastomer. After hole filling, additional elastomer was applied at the interface between adjacent foam blocks, which were then assembled into a layered structure. This assembly step could be performed either sequentially or independently of the hole-filling process.

For the foambots used in the bending angle test (Figure 2), unpatterned foam blocks were attached to both ends of the patterned foam structure. For those used in the inverse design calculation (Figure 3), elastomer plates were attached to each end. These plates were fabricated by casting elastomer into a 3D-printed mold with a reservoir size of 20 mm × 20 mm × 1.2 mm.

Fabrication of Buoyancy Block

The elastomer shell for the buoyancy block was fabricated via a molding process. The mold consisted of two 3D-printed PLA pieces. For the large buoyancy block used for modular floating assistants, the mold included a wall piece and a bottom piece, whereas for the small buoyancy block, it consisted of a cover piece and a bottom piece. After assembling the mold components, elastomer (Ecoflex 00-30, Smooth-On) was injected into the cavity. Once the elastomer was fully cured, the mold was disassembled, and the elastomer shell was retrieved.

As the filling material, we used sponge blocks that were expanded by wetting and then dried, providing both low weight and adequate stiffness. For small buoyancy blocks used for the foamboat, shells with dried sponge blocks were then positioned on a 3D-printed cover mold pre-filled with elastomer to seal the structure. For large buoyancy blocks used for the modular floating assistants, covers were fabricated separately using 3D-printed mold and attached on the shell with dried sponge blocks, using silicone adhesive Sylpoxy, Smooth-On). After the final curing step, the complete buoyancy block was obtained. The dimensions of the large buoyancy block were 110 mm × 70 mm × 20 mm, and those of the small one were 20 mm × 20 mm × 19 mm.

Fabrication of Modular Floating Assistants and Foamboat

For modular floating assistants and foamboat, foambots and buoyancy blocks were prepared separately. as building blocks. To integrate foambots and buoyancy blocks together into one body, silicone adhesive (Sylpoxy, Smooth-On) was utilized between them.

For the modular floating assistants, 9 large buoyancy blocks were connected each other with 3 foambots which were composed of 5 foam blocks. Foambots on the same large buoyancy block were aligned vertically along to the length of the buoyancy block. Permanent magnet disks (15 mm × 3 mm) were encapsulated with elastomer (Ecoflex 00-30, Smooth-on) and were attached on the first and last large buoyancy blocks using silicone adhesive.

For the foamboat, foambots and small buoyancy blocks were glued together with silicone adhesive. U-shaped connector on the center of the foamboat was composed of the array of 16 buoyancy blocks. This connector was linked to the bridge composed of another array of 9 buoyancy blocks via six unpatterned foambots, each consisting of seven foam blocks arranged with three on each side. On the inner curvature of the U-shaped connector, incapsulated permanent magnet disks (15 mm × 2 mm) were installed on the inner curvature, aligned to the magnets on the modular propulsion system. Foambots on the main body were consisted of 7 foam blocks without patten. To reinforce the structural stability during locomotion, arrays of

thicker foam blocks were employed along to the center line of the foamboats, connecting each body part. On the head and tail of the foamboat, combined structures of foambots and small buoyancy robot were utilized to generate closed loop after shape-morphing. On the end of this structure, encapsulated permanent magnet disks (15 mm × 3 mm) were attached using silicone adhesive.

Modular Propulsion System and Controller

The modular propulsion system of the foamboat consisted of housing components and driving components. The housing components comprised the main body, lid, and motor cover, all of which were fabricated by 3D printing using PLA filament. The driving components and controller were sourced from a commercial RC boat (Amazon), including the motor, motor controller, motor driver, propeller with waterproof shaft assembly, and battery. The motor and propeller assembly were mounted on the underside of the housing's main body, and the motor cover was fastened above them using screws. The main body of the housing featured a propeller hole, which was sealed with silicone adhesive (Sylpoxy, Smooth-On) after installation.

To maintain proper weight distribution, the motor driver and battery were aligned in series on top of the motor cover. The housing was precisely fitted to securely hold all components in place without looseness or vibration. To ensure a watertight seal, a gasket rubber was placed between the main body and lid of the housing, which were then fastened with screws. For enhanced reusability and modularity, pairs of permanent magnets were attached to the side walls of the housing main body. To prevent corrosion, these magnets were encapsulated in elastomer through molding.

Characterization of Foambot

For the bending test of the foambot, image processing was conducted to trace the intersection lines between foam blocks. Pictures of each foambot with different hole patterns were taken after bending, and the angle between two extended lines drawn at each intersection was measured. To obtain the line positions, a macro function implemented in a PowerPoint slide was utilized. Each measurement was independently repeated with three different sets of foambots to ensure consistency and reliability, and the error bands represent one standard deviation from the mean.

For the compression test of the foam blocks, a universal testing machine (Instron 5544) was used. Expanded foam blocks in both dry and wet states were compressed along the z-axis in two different orientations: from the top and from the side. Each measurement was conducted

independently four times to ensure consistency and reliability, and the error bands represent one standard deviation from the mean.

Characterization of Buoyancy Block

The static water displacement method with mass correction was used to determine the net buoyancy force of the buoyancy blocks. Two types of five-layers foambots were prepared for testing: one composed of foam blocks without hole patterns and the other composed of buoyancy blocks. Each foambot was gently submerged just beneath the water surface in a volumetric measuring container filled with water using a thin metal wire. The displaced water volume was recorded immediately after the foambot was fully submerged.

The net buoyancy force was calculated by subtracting the apparent weight of the foambot from the weight of the displaced water. The foambot composed of foam blocks was weighed after gently removing only the surface water, without compressing its structure. In contrast, the foambot composed of buoyancy blocks was weighed after the surface water was carefully removed using a wiper. Each measurement was independently repeated five times for three different samples to ensure consistency and reliability, and the error bands represent one standard deviation from the mean.

Finite Element Analysis

Finite element analysis was carried out to predict the bending deformation of the foambot according to its design parameters. The commercially available software COMSOL was used for the simulation. Two different groups of foambots were modeled: six foambots with varying foam block lengths but identical hole positions, and eight foambots with varying hole positions but identical foam block lengths.

Geometric modeling was performed in COMSOL, where the key design parameters included the distance H_1 between the hole and the base surface of the foambot, and the total foambot height L_1. Each foambot was modeled as consisting of one foam block with a hole pattern, two foam blocks without holes, and an elastomeric adhesive layer. To focus the simulation on nonlinear deformation induced by the hole constraint, rather than moisture distribution, simplifications were applied. Specifically, the foambots were modeled in a fully swollen state (20 × 20 × 20 mm), and the elastomer adhesive within the hole was pre-stretched by a factor of 10.

As a result, the adhesive tended to contract toward its original length (2 mm), while the surrounding foam blocks resisted this contraction. The final deformation of the foambot

corresponded to the mechanical equilibrium achieved between these opposing forces. The elastomer adhesive was modeled using Ecoflex 00-30, with its mechanical properties described by a linear elastic model (Young's modulus E = 70 kPa, Poisson's ratio v = 0.495). The foam blocks were modeled as a superelastic material based on the Neo-Hookean model, with mechanical properties defined by E = 6.96 kPa and v = 0.

Inverse Design Calculation

The inverse design calculation proceeded with determining the required number of foam blocks, estimating their corresponding curvature, and computing the hole pattern positions based on these values.

When a discretized spline object was given, it was segmented into piecewise planar curves, each representing an arc on a 2D plane. To determine the number of foam blocks on each segment, the total arc length L_{arc} of the planar curve was first computed from its discretized 2D representation. Given the average arc length l_{arc} of a single foam block, the approximate number of blocks was calculated as $N = L_{arc}/l_{arc}$.

To enable accurate physical construction using an integer number of modules, the input curve was uniformly rescaled such that the resulting value of N fell within ±15% of its nearest integer. This condition ensured that the final value of N lay in the range [n−0.15, n+0.15], where n = round(N), thereby minimizing geometric distortion while preserving design fidelity. The final number of foam blocks was then set to this nearest integer n for physical implementation.

The average curvatures $\kappa_j s$ assigned to each foam block of index j in the coordination were then computed using the discrete formulation from Bergou et al., based on turning angles along a discretized arc segment:

$$\kappa_j = \frac{1}{N_j}\sum_{i=1}^{N_j} 2\tan\left(\frac{\theta_i}{2}\right) \quad (1)$$

Where θ_i denoted the turning angle at vertex i of the discretized curve and N_j indicates the number of vertices corresponding to one foam block within a given segment.[50] The curvature κ represents the total geometric turning within a single foam block and serves as the basis for determining the hole pattern. Given the known relationship between hole position and bending angle (Figure 2c), the curvature of each arc section was matched to a corresponding foam block type (denoted as Dn), where n specifies the hole position from the foam block edge.

For example, to approximate a ring with radius 27.5 mm, the arc length becomes approximately 172.8 mm. Given a swollen foam block length of 11.56 mm, the number of blocks N required is about 14.95. Since this value lies within ±15% of the nearest integer, the arc was implemented using 15 blocks. The curvature for each foam block segment was then calculated using the

discrete turning angle formulation, and the resulting value was converted to a bending angle by geometric inversion. A bending angle of ~24.1°, for instance, would correspond to a D6-type block, as established in the experimental calibration.

This process was repeated to derive the full sequence of block types for each segment. While only integer hole positions ranging from 3 to 10 mm were used in our prototypes, the linear relationship observed between hole position and bending angle allows for finer granularity (e.g., 5.5 mm) in future implementations, offering greater precision in curvature control and structural programming.

This curvature calculation process was applied to each planar segment individually. The results were then merged to construct the complete layer coordination, with appropriate rotations applied to account for the orientation of each segment based on the segmentation plane normals. The final layer coordination were illustrated schematically following the mapping scheme shown in Figure 3b.

Statistical Analysis

We conducted quantitative analysis and characterizations of foambots and buoyancy blocks for the number of independent performances (N). The Ns and units of each measurement were noted in each figure legend and corresponding section of Materials and Methods. The plots in Fig. 2 and fig. S5 shows the mean values, and error bars or shaded regions indicate SD.

Acknowledgements

The work is supported by the US National Science Foundation and the National Research Foundation of Korea. In particular, we thank the Sejong Science Fellowship Grants_Overseas Training Track (RS-2024-00358438) through the National Research Foundation of Korea (NRF) funded by the Ministry of Science and ICT (MSIP) of the Republic of Korea. We also thank the US National Science Foundation grants 2427455 and 2427553.

Conflict of Interest

The authors declare no conflict of interest.

Author Contribution

L.Y. and H.L. contributed to the conceptualization of the study. H.L., T.Y., and M.Z. conducted the fabrication and experimental procedures. H.L. performed the characterization. Y.S. carried

out the simulation. H.L. and D.J. conducted the inverse design calculation. L.Y. supervised the project. L.Y., H.L., D.J., and Y.S. wrote the manuscript.

Received: ((will be filled in by the editorial staff))
Revised: ((will be filled in by the editorial staff))
Published online: ((will be filled in by the editorial staff))

References

1. T. Møretrø, B. Moen, V. L. Almli, et al., "Dishwashing sponges and brushes: Consumer practices and bacterial growth and survival," *Int. J. Food Microbiol.* 337 (2021): 108928. https://doi.org/10.1016/j.ijfoodmicro.2020.108928

2. N. Gao, L. Tang, J. Deng, K. Lu, H. Hou, K. Chen, "Design, fabrication and sound absorption test of composite porous metamaterial with embedding I-plates into porous polyurethane sponge," *Appl. Acoust.* 175 (2021): 107845. https://doi.org/10.1016/j.apacoust.2020.107845

3. Y. Hwang, M. S. B. Ibrahim, J. Deng, J. A. Jackman, N.-J. Cho, "Colloid-mediated fabrication of a 3D pollen sponge for oil remediation applications," *Adv. Funct. Mater.* 31, no. 24 (2021) 2101091. https://doi.org/10.1002/adfm.202101091

4. Y. Shang, R. Gao, Y. Wang, et al., "Scalable fabrication of efficient and recycling wood residue-derived sponge for crude oil adsorption," *J. Hazard. Mater.* 441 (2023): 129979. https://doi.org/10.1016/j.jhazmat.2022.129979

5. M. J. Azuraini, S. Vigneswari, K.-H. Huong, et al., "Surface modification of sponge-like porous poly(3-hydroxybutyrate-co-4-hydroxybutyrate)/gelatine blend scaffolds for potential biomedical applications," *Polymers* 14, no. 9 (2022): 1710. https://doi.org/10.3390/polym14091710

6. T. Jiang, S. Chen, J. Xu, et al., "Superporous sponge prepared by secondary network compaction with enhanced permeability and mechanical properties for non-compressible hemostasis in pigs," *Nat. Commun.* 15 (2024): 5460. https://doi.org/10.1038/s41467-024-49578-2

7. S. Meng, N. Wu, J. Fang, et al., "Construction of a biomimetic tubular scaffold inspired by sea sponge structure: Sponge-like framework and cell guidance," *Adv. Sci.* 12, no. 16 (2025): 2416627. https://doi.org/10.1002/advs.202416627

8. J. Ha, J. Kim, Y. Jung, G. Yun, D.-N. Kim, H.-Y. Kim, "Poro-elasto-capillary wicking of cellulose sponges," *Sci. Adv.* 4, no. 3 (2018): eaao7051.
https://doi.org/10.1126/sciadv.aao7051

9. Y. Cui, Y. Wang, Z. Shao, A. Mao, W. Gao, H. Bai, "Smart sponge for fast liquid absorption and thermal responsive self-squeezing," *Adv. Mater.* 32, no. 14 (2020): 1908249.
https://doi.org/10.1002/adma.201908249

10. J. Bern, P. Banzet, R. Poranne, S. Coros, "Trajectory optimization for cable-driven soft robot locomotion," in *proceedings of* Robotics: Science and Systems (RSS 2019), vol. 1 (2019): 1-8.
https://doi.org/10.15607/RSS.2019.XV.052

11. M. Coelho, H. Ishii, P. Maes, "Surflex: a programmable surface for the design of tangible interfaces," in *proceedings of* CHI*'08 Extended Abstracts on Human Factors in Computing Systems* (2008): 3429–3434.
https://doi.org/10.1145/1358628.1358869

12. H. Xu, X. Wang, Y. Nan, et al., "Flexible sponge-based nanogenerator for energy harvesting from land and water transportation," *Adv. Funct. Mater.* 33, no. 49 (2023): 2304723.
https://doi.org/10.1002/adfm.202304723

13. J. Wang, Q. Zhou, A. Wang, et al., "Sponge inspired flexible, antibacterial aerogel electrode with long-term high-quality electrophysiological signal recording for human-machine interface," *Adv. Funct. Mater.* 34, no. 23 (2024): 2309704.
https://doi.org/10.1002/adfm.202309704

14. J. Kim, J. Deng, N.-J. Cho, S. M. Han, "Directional, silanized plant-based sponge for oil collection," *Adv. Funct. Mater.* 34, no. 23 (2024): 2313808.
https://doi.org/10.1002/adfm.202313808

15. H. Guan, R. Lian, R. Li, et al., "A low-temperature carbonization strategy for efficient viscous crude oil spill disposal without hydrophobic coating: CoFe-PBA-catalyzed carbonization of superhydrophobic flame retardant melamine sponge," *Adv. Funct. Mater.* 34, no. 14 (2023): 2313224.
https://doi.org/10.1002/adfm.202313224

16. D. Zhu, J. Lu, M. Zheng, D. Wang, J. Wang, Y. Liu, X. Wang, M. Zhang, "Self-powered bionic antenna based on triboelectric nanogenerator for micro-robotic tactile sensing," *Nano Energy* 114 (2023): 108644.
https://doi.org/10.1016/j.nanoen.2023.108644

17. Y. Yang, H. Zhang, F. Zeng, Q. Jia, L. Jiang, A. Yu, B. Duan, "A quaternized chitin derivatives, egg white protein and montmorillonite composite sponge with antibacterial and hemostatic effect for promoting wound healing," *Compos. B: Eng.* 234 (2022): 109661. https://doi.org/10.1016/j.compositesb.2022.109661

18. N. Ono, R. Seishima, K. Okabayashi, H. Imai, S. Fujii, Y. Oaki, "Stimuli-responsive sponge for imaging and measuring weak compression stresses," *Adv. Sci.* 10, no. 3 (2022): 2206097. https://doi.org/10.1002/advs.202206097

19. X. Cui, Z. Liu, B. Zhang, et al., "Sponge-like, semi-interpenetrating self-sensory hydrogel for smart photothermal-responsive soft actuator with biomimetic self-diagnostic intelligence," *Chem. Eng. J.* 467 (2023): 143515. https://doi.org/10.1016/j.cej.2023.143515

20. W. Zhiheng, D. Yimin, F. Chengqian, et al., "A bio-inspired green method to fabricate pH-responsive sponge with switchable surface wettability for multitasking and effective oil-water separation," *Appl. Surf. Sci.* 602 (2022): 154192. https://doi.org/10.1016/j.apsusc.2022.154192

21. K. C. Galloway, K. P. Becker, B. Phillips, et al., "Soft robotic grippers for biological sampling on deep reefs," *Soft Robot.* 3, no. 1 (2016): 23–33. https://doi.org/10.1089/soro.2015.0019

22. Z. Liang, L. Ma, X. Liu, H. Huang, "Sponge-based mobile soft robot with multimodal locomotion," in *proceedings of Cognitive Computation and Systems. ICCCS 2022. Communications in Computer and Information Science*, vol. 1732, ed. F. Sun, J. Li, H. Liu, Z. Chu (2023): 291-298. https://doi.org/10.1007/978-981-99-2789-0_25

23. W. Felt, M. A. Robertson, J. Paik, "Modeling vacuum bellows soft pneumatic actuators with optimal mechanical performance," in *proceedings of 2018 IEEE International Conference on Soft Robotics (RoboSoft)* (2018): 431–436. https://doi.org/10.1109/ROBOSOFT.2018.8405381

24. Y. Yamada, T. Nakamura, "Actuatable flexible large structure using a laminated foam-based soft actuator," in *proceedings of 2020 IEEE/SICE International Symposium on System Integration (SII)* (2020): 74–79. https://doi.org/10.1109/SII46433.2020.9026003

25. T. Mitsuda, S. Otsuka, "Active bending mechanism employing granular jamming and vacuum-controlled adaptable gripper," *IEEE Robot. Autom. Lett. 6*, no. 2 (2021): 3041–3048.

https://doi.org/10.1109/LRA.2021.3058914

26. T. Yue, T. L. You, H. Philamore, H. Bloomfield-Gadêlha, J. M. Rossiter, "A silicone-sponge-based variable-stiffness device," in *proceedings of 2023 IEEE International Conference on Robotics and Automation (ICRA)* (2023): 627-633.
https://doi.org/10.1109/ICRA48891.2023.10160915

27. X. Yao, H. Chen, H. Qin, Q.-H. Wu, H.-P. Cong, S.-H. Yu, "Solvent-adaptive hydrogels with lamellar confinement cellular structure for programmable multimodal locomotion," *Nat. Commun.* 15, (2024): 9254.
https://doi.org/10.1038/s41467-024-53549-y

28. Z. Wang, H. Hu, Z. Chai, et al., "Bioinspired hydrophobic pseudo-hydrogel for programmable shape-morphing," *Nat. Commun.* 16, (2025): 875.
https://doi.org/10.1038/s41467-025-56291-1

29. I. M. Van Meerbeek, C. M. De Sa, R. F. Shepherd, "Soft optoelectronic sensory foams with proprioception," *Sci. Robot.* 3, no. 24 (2018): eaau2489.
https://doi.org/10.1126/scirobotics.aau2489

30. I. M. Van Meerbeek, B. C. Mac Murray, J. W. Kim, et al., "Morphing metal and elastomer bicontinuous foams for reversible stiffness, shape memory, and self-healing soft machines," *Adv. Mater.* 28, no. 14 (2016): 2801-2806.
https://doi.org/10.1002/adma.201505991

31. A. Miriyev, K. Stack, H. Lipson, "Soft material for soft actuators," *Nat. Commun.* 8 (2017): 596.
https://doi.org/10.1038/s41467-017-00685-3

32. T. Huang, R. Wei, Q. Hua, Z. Yuan, G. Shen, "A smart sponge with pressure–temperature dual-mode sensing for packaging and transportation," *Chem, Eng. J.* 499 (2024): 156292.
https://doi.org/10.1016/j.cej.2024.156292

33. J. Hui, F. Xu, Q.-Q. Ni, "Temperature-stimulated phase switching in a novel reversible morphing shape memory sponge for soft robotic actuators," *Chem, Eng. J.* 505 (2025): 159177.
https://doi.org/10.1016/j.cej.2024.159177

34. H. Kaimoto, J. Yamaoka, S. Nakamaru, Y. Kawahara, Y. Kakehi, "ExpandFab: Fabricating objects expanding and changing shape with heat," in *proceedings of TEI '20: Proceedings of the Fourteenth International Conference on Tangible, Embedded, and Embodied Interaction* (2020): 153-164.
https://doi.org/10.1145/3374920.3374949

35. M. L. Dezaki, M. Bodaghi, “Soft magneto-responsive shape memory foam composite actuators,” *Macromol. Mater. Eng.* 307, no. 11 (2022): 2200490.
https://doi.org/10.1002/mame.202200490

36. Y. Yamada, “Feasibility study on botanical robotics: Ophiocordyceps-like biodegradable laminated foam-based soft actuators with germination ability,” *IEEE Robot. Autom. Lett.* 6, no. 2 (2021): 3777–3784.
https://doi.org/10.1109/LRA.2021.3061355

37. Y. Fu, C. Yang, B. Zhang, et al., “A highly sensitive, conductive, and flexible hydrogel sponge as a discriminable multimodal sensor for deep-learning-assisted gesture language recognition,” *Adv. Funct. Mater.* 35, no. 10 (2025): 2416453.
https://doi.org/10.1002/adfm.202416453

38. M. Sheng, Z. Xiao, S. Deng, et al., “A super water-stable polyaniline sponge sensor for multifunctional sensing of physical and chemical stimuli,” *Sens. Actuat. A: Phys.* 387 (2025): 116398.
https://doi.org/10.1016/j.sna.2025.116398

39. G. Mogli, M. Costantini, S. Stassi, “Highly sensitive PDMS-Ag nanoflakes porous pressure sensors prepared by templating and molding approaches for wearable applications,” *Sens. Actuat. A: Phys.* 392 (2025): 116734.
https://doi.org/10.1016/j.sna.2025.116734

40. S. Kim, D. Yoo, J. Lim, J. Kim, “Simple and effective patterning method of liquid-metal-infused sponge electrode for fabricating 3D stretchable electronics,” *Adv. Mater. Technol.* 9, no. 14 (2024): 2301589.
https://doi.org/10.1002/admt.202301589

41. F. Soto, A. Tsui, S. Surappa, et al., “Programmable shape morphing metasponge,” *Adv. Intell. Syst.* 5, no. 8 (2023): 2300043.
https://doi.org/10.1002/aisy.202300043

42. E. Mutlutürk, D. Özbek, O. Özcan, G. B. Demirel, B. Baytekin, “Single-material solvent-driven polydimethylsiloxane sponge bending actuators,” *Soft Robot.* 11, no. 5 (2024): 812-820.
https://doi.org/10.1089/soro.2023.0147

43. W. Yang, W. Li, Y. Lei, P. He, G. Wei, L. Guo, “Functionalization of cellulose-based sponges: Design, modification, environmental applications, and sustainability analysis,” *Carbohydr. Polym.* 348 (2025): 122772.
https://doi.org/10.1016/j.carbpol.2024.122772

44. D. Lang, G. Liu, R. Wu, et al., "Efficient preparation of anisotropic cellulose sponge from cotton stalks: An excellent material for separation applications," *J. Hazard. Mater.* 476 (2024): 134941.
https://doi.org/10.1016/j.jhazmat.2024.134941
45. Y. Alsaid, S. Wu, D. Wu, et al., "Tunable sponge-like hierarchically porous hydrogels with simultaneously enhanced diffusivity and mechanical properties," *Adv. Mater.* 33, no. 20 (2021): 2008235.
https://doi.org/10.1002/adma.202008235
46. W. Zhai, J. Jiang, C. B. Park, "A review on physical foaming of thermoplastic and vulcanized elastomers," *Polym. Rev.* 62, no. 1 (2022): 95-141.
https://doi.org/10.1080/15583724.2021.1897996
47. D. Zong, X. Zhang, X. Yin, et al., "Electrospun fibrous sponges: Principle, fabrication, and applications," *Adv. Fiber Mater.* 4, (2022): 1434-1462.
https://doi.org/10.1007/s42765-022-00202-2
48. C. Katrilaka, N. Karipidou, N. Petrou, et al., "Freeze-drying process for the fabrication of collagen-based sponges as medical devices in biomedical engineering," *Materials* 16, no. 12 (2023): 4425.
https://doi.org/10.3390/ma16124425
49. S. Zou, Y. Li, H. Jin, et al., "Highly safe, durable, adaptable, and flexible fuel cell using gel/sponge composite material," *Adv. Energy Mater.* 12, no. 6 (2021): 2103178.
https://doi.org/10.1002/aenm.202103178
50. M. Bergou, M. Wardetzky, S. Robinson, B. Audoly, E. Grinspun, "Discrete elastic rods," in *proceedings of ACM SIGGRAPH 2008 papers (SIGGRAPH '08)*, Article no. 63 (2008): 1–12.
https://doi.org/10.1145/1399504.1360662

Supporting Information

Supporting Information is available from the Wiley Online Library or from the author.

Table of Contents

Programmable Sponge for Hydro-Active Morphing Module with Light Weight and High-Volume Change

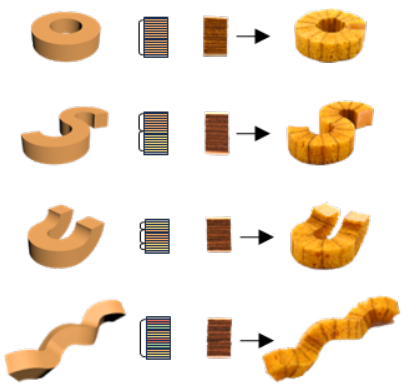

This work introduces a modular shape-morphing system built from cellulose sponge blocks. Upon hydration, programmed swelling induces bending and enables the construction of aquatic devices, including wearable flotation modules and a self-propelling foamboat. The approach leverages sustainable materials and simple fabrication for untethered, reconfigurable deployment in real-world environments.

Supporting Information

Programmable Sponge for Hydro-Active Morphing Module with Light Weight and High-Volume Change

*Hajun Lee, Tianyu Yu, Mingjie Zheng, David Jordan, Yuxuan Sun and Lining Yao**

* Corresponding Author E-mail: liningy@berkeley.edu

This Supporting Information includes:

Other Supplementary Materials for this manuscript include the following:

Movie S1. Swelling process of D6 and D10 foam blocks.
Movie S2. Swelling process of foambot for ring shape.
Movie S3. Swelling process of foambot for letter “S” shape.
Movie S4. Swelling process of foambot for horseshoe shape.
Movie S5. Swelling process of foambot for helix shape.
Movie S6. Swelling and self-locking process of MFA.
Movie S7. Swelling process of the foamboat after deployment.
Movie S8. Forward Locomotion of foamboat.

Supplementary Note

Note S1. Bending angle analysis.

For the bending angle analysis, image processing was conducted on pictures of foambots with varying design parameters to calculate their bending angles. Lines were drawn at the intersections of each foam layer using PowerPoint, and the coordinates of the endpoints of these lines were extracted using the macro script. Since line objects in PowerPoint are not vector-based and the macro script could not correctly identify coordinate pairings for inclined lines, the extracted coordinates for such lines were initially recorded as (x_1, y_2) and (x_2, y_1), instead of (x_1, y_1) and (x_2, y_2). To address this, the coordinate pairs were manually corrected by exchanging the y-coordinates of each point after data extraction. As a result, four coordinate points were obtained from two lines per foambot sample: (x_1, y_1) and (x_2, y_2) from line 1, and (x_3, y_3) and (x_4, y_4) from line 2. These points enabled the calculation of the bending angle between these two lines using Equation (1).

$$\theta = arccos\left(\frac{(x_2 - x_1)(x_4 - x_3) + (y_2 - y_1)(y_4 - y_3)}{\sqrt{(x_2 - x_1)^2 + (y_2 - y_1)^2}\sqrt{(x_4 - x_3)^2 + (y_4 - y_3)^2}}\right) \quad (1)$$

Supplementary Figures

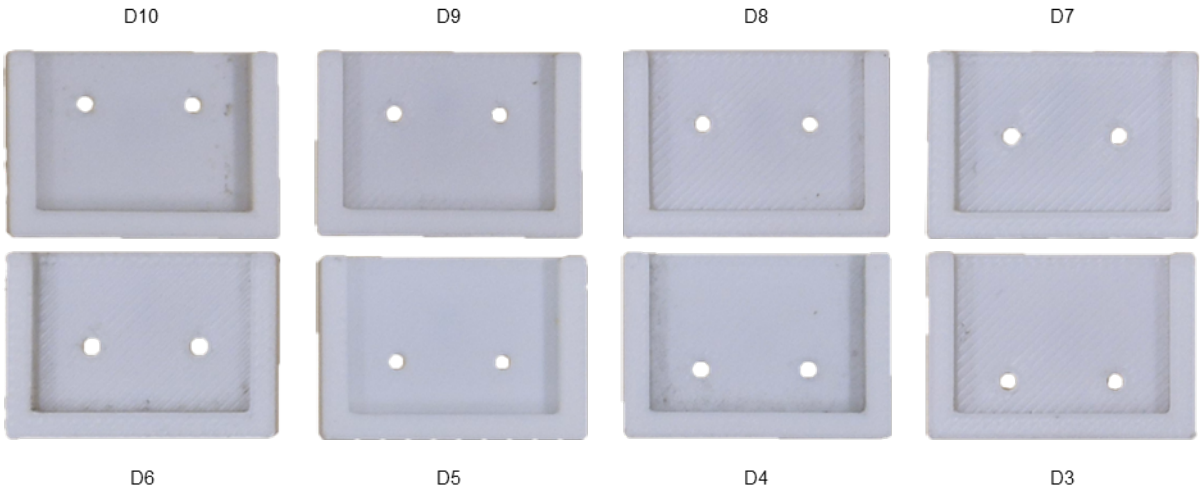

Figure S1. Hole template with various hole patterns. 3D printed hole templates with 3–10 mm hole patterns.

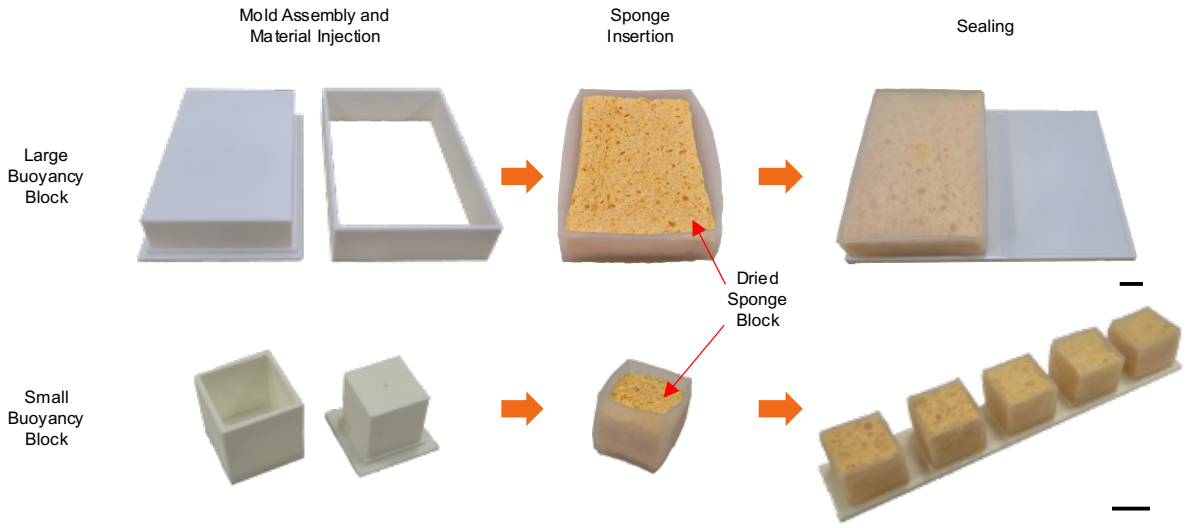

Figure S2. Fabrication process of buoyancy block. Both large and small buoyancy blocks were fabricated using a molding technique. After assembling each mold component, liquid elastomer was injected into the mold. Once fully cured, the elastomer shell was demolded, and a dried sponge block was inserted into the cavity. For the large buoyancy block, a thin elastomer film was first cast using the cover mold. The shell containing the sponge was then bonded to the film using a silicone adhesive to seal the opening. For the small buoyancy block, the cover mold was pre-filled with liquid elastomer, and the elastomer shell with the sponge inside was placed directly into the mold. After curing, the completed buoyancy blocks were retrieved from the mold. Scale bars, 1 cm.

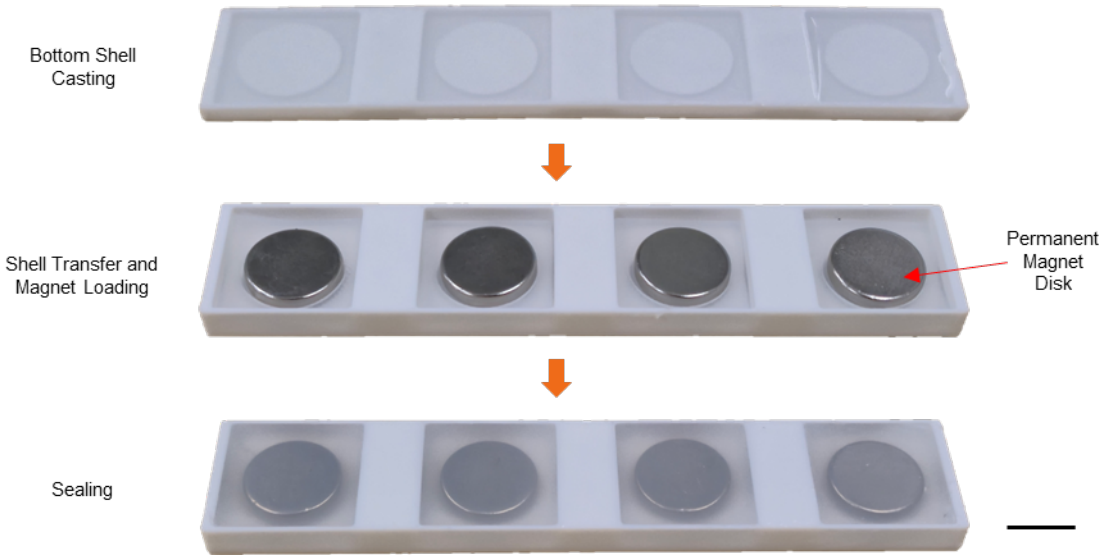

Figure S3. Fabrication process of magnetic block with elastomer shell. Magnetic blocks used for the self-locking mechanisms in the Modular Floating Assistants (MFAs) and the foamboat were fabricated via a two-step molding process. First, bottom elastomer shells were cast using a mold featuring a central cavity to accommodate a permanent magnet. After curing, the shells were transferred to a secondary mold with a deeper cavity, where permanent magnet disks were placed at the center. Additional elastomer was then poured over the magnets and cured to fully encapsulate them. Scale bar, 1 cm.

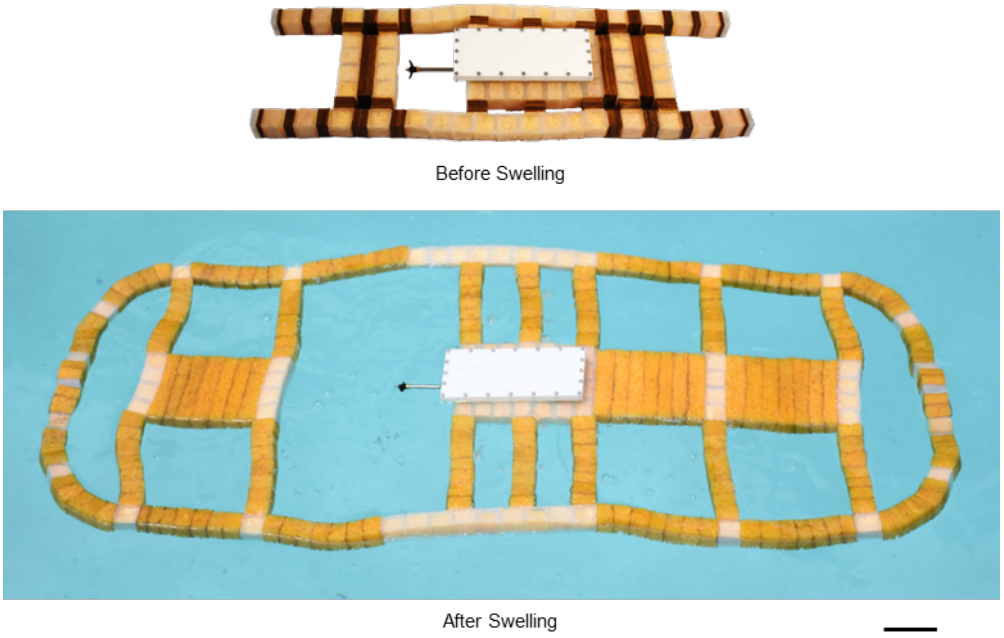

Figure S4. Foamboat integrated with modular propulsion system before and after swelling. Foamboat and modular propulsion system can be integrated with four magnet blocks installed on the U-shaped connector of foamboat and side wall of modular propulsion system. Scale bar, 5 cm.

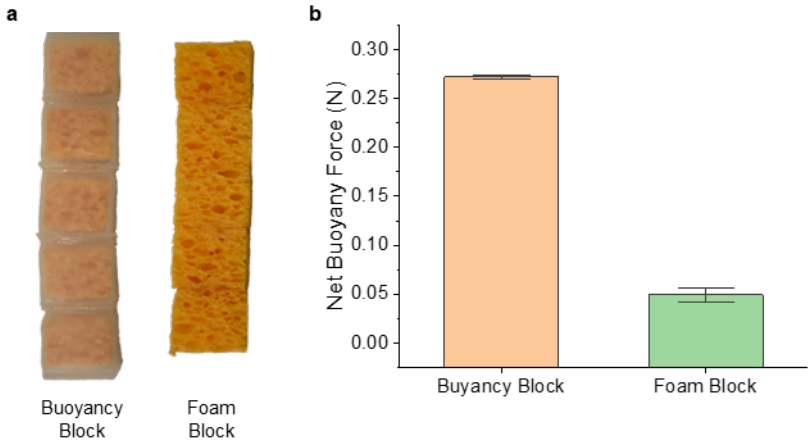

Figure S5. Buoyancy comparison between small buoyancy block and foam block without elastomer shell. Net buoyancy force of small buoyancy block and foam block. a) Picture of samples used on buoyancy measurement, composed of 5 small buoyancy blocks and 5 foam blocks without hole pattern respectively. b) Net buoyancy force provided by buoyancy blocks and foam blocks. For statistical testing, N = 5 (five independent samples, each tested three times), and the data with error bars are presented as mean ± SD.

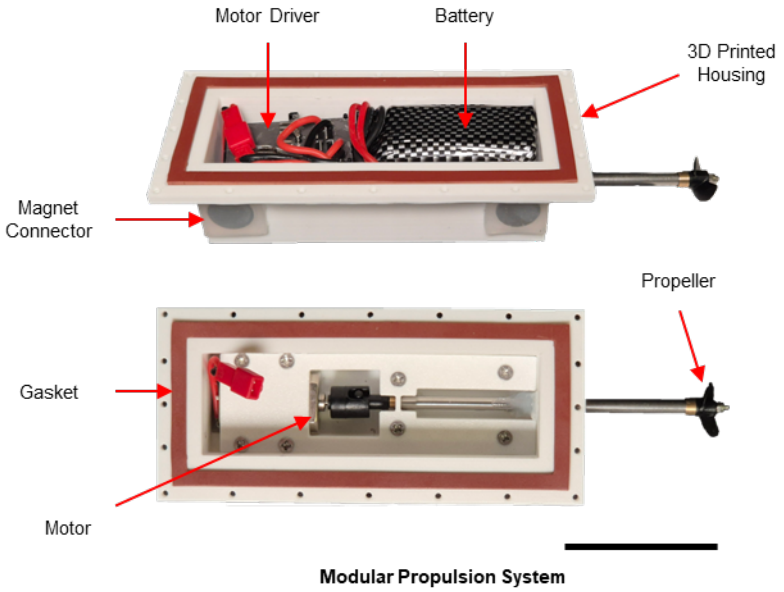

Figure S6. Components of modular propulsion system. Scale bar, 5 cm.